2023 IEEE International Conference on Robotics and Automation (ICRA 2023)
May 29 - June 2, 2023. London, UK

MagTac: Magnetic Six-Axis Force/Torque Fingertip Tactile Sensor for Robotic Hand Applications

Sungwoo Park, Sang-Rok Oh, and Donghyun Hwang, *Member, IEEE*

***Abstract*—We develop a novel hall-effect-based six-axis force/torque (F/T) tactile sensor integrated into the fingertip of robotic hands. When the robotic hands performs the grasping tasks in an unstructured environment, the visual information plays a main role in sensing the external properties of the objects. However, the various intrinsic properties of the objects such as softness, roughness, mass distribution, and weight cannot be measured properly only with the visual information. To detect the various force information in performing diverse tasks, we aim to implement the six-axis F/T fingertip tactile sensor with hall-effect-based principle. The experimental results demonstrate that the proposed sensor can measure the six-axis F/T with average errors of about 3.3 %. In addition, it is observed that the effect of stray field can be shielded by applying a soft magnetic shielding film to the sensor.**

I. Introduction

Robotic hands usually perform grasping and manipulation tasks in structured environments with pre-trained objects. This is because visual information has been conventionally used as major information in various tasks [1], [2]. Visual information can sense the external properties of objects such as absolute position, shape, size, and posture. However, when the robotic hand operates the task in an unstructured environment, there exists a limitation to performing the tasks only with visual feedback. This is because the intrinsic properties that aid to grasp and manipulate the object, such as softness, roughness, mass distribution, and weight information, cannot be detected by the visual information. Therefore, the various sensing information for providing additional details of the object's properties is necessary.

A tactile sensor can play a prominent role in detecting the intrinsic properties of the object which are hard to be detected only by visual information. In addition, the various force information sensed by the tactile sensor can help the robotic hands to perform variety of tasks such as manipulating objects [3], [4] and grasping delicate objects [5], [12]. For this aim, many types of tactile sensors that can measure the external forces and stimuli have been developed via various sensing principles such as barometric [5], capacitive [6], optical [7]-[9], piezoresistive [10], [11] and hall-effect [11]-[22].

This work was supported in part by the National Research Foundation of Korea (NRF) grant funded by the Korea government (MSIT) under Grant 2020R1A2C2100193, in part by the Korea Advanced Research Program through the National Research Foundation of Korea (NRF) funded by Ministry of Science and ICT under Grant 2020M3H8A1115029, and in part by the Korea Institute of Science and Technology (KIST) Institutional Program. (Corresponding author: Donghyun Hwang.)

The authors are with the Center for Robotics Research, KIST, Seoul 02792, South Korea. (Corresponding author's e-mail: donghyun@kist.re.kr)

Sungwoo Park is also with the School of Electrical Engineering, Korea University, Seoul 02841, South Korea.

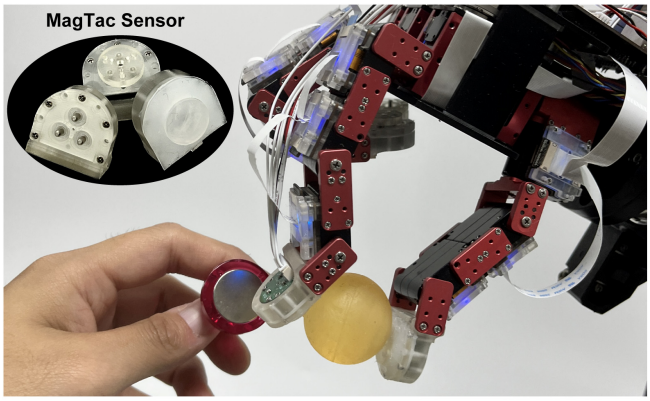

Fig. 1. The proposed MagTac sensor capable of measuring the six-axis force/torque based on the hall-effect sensing principle.

Nonetheless, most of the sensors are limited to measuring the forces in different directions.

In our previous work, we developed a three-dimensional arrayed tactile sensor capable of sensing distributed force with the barometric pressure sensor, but it still has a shortcoming of measuring unidirectional normal force [5]. A capacitive type tactile sensor consisting of 36 nibs to detect the linear and rotational slip is developed, and this can work as the six-axis F/T sensor. However, the repeatability of the sensor is degraded depending on how the nibs bend in response to the load [6]. In the case of the optical-based tactile sensors adopting the camera, while they can measure the normal and shear directional forces with high resolution, it has a limited measurement capacity of forces with a low sampling rate [7], [8]. Another approach of using a photodiode-based tactile sensor has been developed, but it still has a limitation in measuring the external torque [9]. A piezoresistive type tactile sensor was developed with high sampling rate. However, it only measures single directional normal force [10]. In addition, a hybrid type that can achieve skin-like perception is proposed, but it has a limited measurement capacity [11].

Compared to these sensing principles, a hall-effect-based tactile sensor is a promising technology to be integrated into confined spaces with multi-directional measurement capability. However, the lack of six-axis F/T measurement capability [12]-[22], interaction with the ferromagnetic material [12], [13], [15]-[22] and vulnerability to external stray field [12]-[16], [18]-[22] still remains as the problems to be solved. The comparison of the previous studies of the tactile sensors and our proposed sensor is tabulated in Table I.

Considering the limitation of the former studies, we develop a hall-effect-based tactile sensor that can achieve six-axis F/T measurement and immunity to the stray magnetic field. Fig. 1 shows the proposed MagTac sensor employed on robotic hand.

TABLE I. COMPARISON OF PREVIOUSLY STUDIED TACTILE SENSORS AND OUR PROPOSED SENSOR

Reference	Type of the sensor	F/T measurement capability			Max. sampling rate
		F_z	F_x, F_y	T_x, T_y, T_z	
[5]	Barometric pressure	1.47 N	×	×	330 Hz
[6]	Capacitive	15 N	3.5 N	50 N·mm	300 Hz
[7]	Optical with CCD camera	2.5 N	1.7 N	×	-
[8]	Optical with LED and RGB camera	2 N	○ (Not reported)	×	10 Hz
[9]	Optical with photodiode	11 N	4 N	×	1000 Hz
[10]	Piezoresistive	140 kPa	×	×	4000 Hz
[11]	Piezo resistive and hall effect with neodymium magnet	2 N	○ (Not reported)	×	250 Hz
[12]	Hall effect with magnetic film	8 N	F_x: 1 N	×	130 Hz
[13]	Hall effect with magnetic film	○ (Not reported)	×	×	-
[14]	Hall effect with ferromagnetic film	2.5 N	×	×	200 Hz
[15]	Hall effect with neodymium magnet	50 N	×	×	-
[16]	Hall effect with neodymium magnet	32 N	0.5 N	×	-
[17]	Hall effect with neodymium magnet	3.5 N	0.8 N	T_x, T_y: 60 N·mm	-
[18]	Hall effect with neodymium magnet	20 N	3 N	×	2000 Hz
[19]	Hall effect with neodymium magnet	2.6 N	0.4 N	×	-
[20]	Hall effect with neodymium magnet	×	×	×	340 Hz
[21]	Hall effect with neodymium magnet	×	×	×	-
[22]	Hall effect with neodymium magnet	14 N	2 N	×	500 Hz
MagTac	**Hall effect with neodymium magnet**	**32 N**	**15 N**	**250 N·mm**	**2000 Hz**

II. CONCEPT AND WORKING PRINCIPLE

A. Structure and Sensing Mechanisms

Fig. 2 illustrates the structure and sensing mechanism of the single-cell MagTac sensor. The sensor is composed of flexure and pillar, which generate the motion in accordance with the applied force in the normal and shear direction. Additionally, the permanent magnet with thickness of 1 mm and diameter of 2 mm (NdFeB-8321, Radial Magnets) is embedded inside the pillar. When an external force is applied to the pillar, the magnetic sensor (MLX90395, Melexis) attached to the PCB senses the difference in magnetic flux density according to the relative position and posture of the magnet as shown in Fig. 2(g-1).

As illustrated in Fig. 2(b), an external normal force changes magnetic flux density as the relative position of the magnet changes. In this state, the magnitude of the magnetic flux density (B_{norm}) change is calculated as follows:

$$B_{norm} = \sqrt{(B_x - B_{x0})^2 + (B_z - B_{z0})^2} \tag{1}$$

where, (B_{x0}, B_{z0}) denotes the magnetic flux density at the initial state; and (B_x, B_z) denotes the magnetic flux density at the deformed state when a normal force is applied. Unlike the normal direction force, the external shear force applied to the pillar changes the relative posture of the magnet which causes the magnetic flux density to change. Fig. 2(c) schematically depicts the deformation characteristic caused by the external shear force. The magnet rotates with respect to the pivot point with angle θ and this can be calculated by the magnetic field ratio change which can be expressed as:

$$\theta = \arctan\left(\frac{B_x - B_{x0}}{B_z - B_{z0}}\right) \cdot \tag{2}$$

From (1) and (2), the external normal and shear force can be calculated by the relative position and posture of the magnet. Furthermore, the ratio of the pillar length (L_1/L_2) affects the shear direction sensitivity, increased ratio results in higher sensitivity (see Fig. 2(g-2)). However, the increased ratio of the pillar length also increases the parasitic displacement ε in the z-direction by the rotational motion of the pillar. To reduce the parasitic displacement errors, the relationship between the position and posture of the magnet needs to be calculated as:

$$\varepsilon = r - r\left|\cos(\theta)\right| \tag{3}$$

where, r is the distance between the pivot point and the magnet. Using (1), (2), and (3), our proposed sensor can calculate the normal and shear directional external force using the relationship between magnetic flux density and forces. Moreover, the shear direction sensitivity can be tuned at the structure in the designing stage of the sensor.

B. Structural Design and Analysis

In order to obtain a highly reliable signal due to the deformation, a motion-guided mechanism is necessarily required. However, since the tactile sensors are usually embedded in confined spaces, the mechanical components to accurately guide the motion are usually bulky. To overcome this problem, we propose the flexure structure which can reduce the overall volume of the required mechanical components and enhance the sensing performance. Considering the advantages, the flexure structure is designed and applied to our proposed sensor.

Among the various type of motion-guiding flexure, the diaphragm flexure structure is selected as a proper model in our sensor design. This is because the diaphragm flexure structure can compactly be arranged and offers three Degrees of Freedom (DoF) with the desired direction and three Degrees of Constraint (DoC) with the undesired direction in our sensor design. The diaphragm flexure structure is comprised of a fixed outer frame, intermediate flexure, and internal moving part as shown in Fig. 2(d-1). Note that the intermediate layer of the diaphragm flexure is built up of multiple single-strip flexures.

To determine the proper parameter of the diaphragm flexure structure, we first analyze the relationship between the

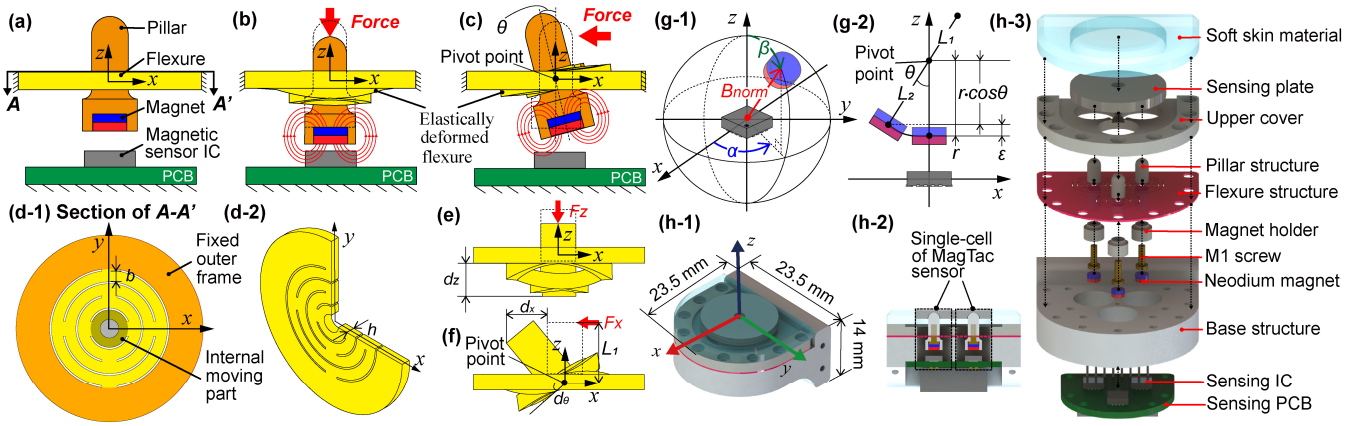

Fig. 2. Structural configuration and the working principle of the MagTac. (a) represents the configuration of the single-cell MagTac sensor. (b) and (c) are the deformation characteristic according to the normal and shear force, respectively. (d) is the design and the mechanical model of the flexure structure. (e) and (f) are the displacements by applied normal and shear forces, respectively. (g-1) and (g-2) show the polar coordination of magnetic field intensity according to the relative position and posture of the permanent magnet. (h-1) and (h-2) are isometric views and the sectional view of the rendered images of the MagTac sensor, respectively. (h-3) represents the components of the MagTac sensor.

force and deformation. As shown in Fig. 2(e), the normal deformation (d_z) of the inner moving part according to the applied normal force (F_z) is described as [23]:

$$d_z = \frac{(nc - 2\pi r_f)^3}{12 n^4 E I} F_z \tag{4}$$

where, I is the moment of inertia of an individual flexure, which can be expressed as $I = bh^3/12$ in other term. c and r_f denote the tangential distance between the flexures and the mean radius of the flexure, respectively. n and E represent the number of flexures in the diaphragm and the modulus of elasticity, respectively.

The relationship between the shear force and the flexure deformation is depicted in Fig. 2(f). The rotational deformation (d_θ) according to the shear force (F_x) is derived as follows [24]:

$$d_\theta = \frac{2\pi r_f - nc}{n(2Gbh(1/3) - 0.21(h/b)[1-(1/12)(h/b)^4])} L_1 F_x \tag{5}$$

where, G and L_1 denote the shear modulus of the material and the linear distance between the contact point and pivot point, respectively.

The simulation results verify that both normal and rotational deformation highly affects to the diaphragm flexure thickness h as shown in Fig. 2(d-2). To determine the feasible design parameter, we prepare several samples with different thicknesses and conduct the static and modal analysis based on the finite element method (FEM) using simulation software (Workbench 18.2, ANSYS) as displayed in Fig. 3. The material of the flexure structure is determined as polyoxymethylene (POM) for the large deflection, which has an elastic modulus of 2660 MPa and tensile strength of 59.5 MPa. Considering the arrangement interval between each sensing cell, the related parameters to the outer radius of the flexure (e.g. c, r_f, n, and b) are fixed. This is because the closer the distance between each sensing cell is, the larger the magnetic interference becomes by the adjacent magnet. On the other hand, as the distance becomes larger, the dead zone which degrades the localization accuracy of the tactile sensor also increases. As a result, considering the minimum arrangement interval and magnetic interference by simple experiments, the dimensions of the radius and arrangement interval of the flexure are set to 6.4 and 7 mm, respectively.

Fig.3 (a) and (b) show the simulation results for the stress and deformation of the flexure structure when 1 N force is applied in the normal and shear direction. In the simulation, the outer frame is fixed, and the external force is applied to the pillar on the internal moving part. Static analysis is conducted with different flexure thicknesses h and the results are shown in Fig. 3 (c), (d), and (e). In addition, Fig. 3(f) denotes the modal analysis result. The amount of deformation d_z and d_x are obtained under an applied 1 N normal and shear directional force. The FEM simulation results show that the maximum deformation of normal and shear directions is decreased exponentially as flexure thickness increases. Moreover, the normal and shear direction stiffness, and resonant frequency increased accordingly. Based on the FEM simulation result, we determine the thickness of the flexure as 1 mm.

The radial symmetrical design of the flexure structure can reduce the time-consuming effort in proceeding calibration to improve sensing performance. To identify the stiffness of each direction, we calculate the normal and shear direction stiffness using the relationship between applied force and maximum deformation. The simulation results in Fig. 3(e) demonstrate that the flexure structure has an almost symmetrical stiffness in the x-, y-directions.

C. Fabrication of MagTac Sensor

Fig. 2(h) shows the overall components and structure of the proposed sensor. The flexure structure is machined by the commercial laser cutting machine (Speedy100, Trotec) and the other five components (i.e. base structure, magnet holder, pillar structure, upper cover, sensing plate) are three-dimensionally printed with ABS material. The printed parts are assembled by the mechanical bolt. Then, a soft skin material (Mold Star 31T, SMOOTH-ON) is bonded on the top of the sensing plate and upper cover by the silicone rubber adhesive (Sil-Poxy, SMOOTH-ON).

III. Experimental Results

The conceptually designed MagTac sensor is fabricated as a functional prototype. In this section, the experimental

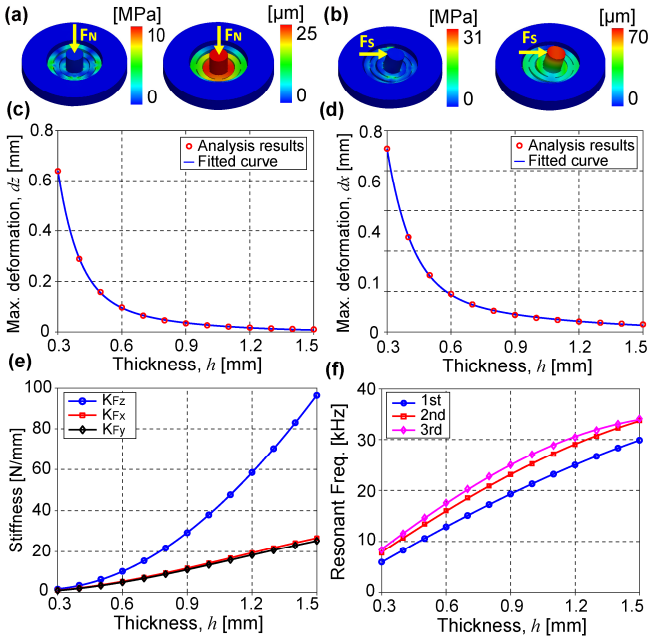

Fig. 3. Finite element method (FEM) simulation results of the single flexure structure embedded in the MagTac. (a) and (b) are the equivalent stress and deformation by an external normal and shear force, respectively. (c) and (d) indicate the static analysis results of the maximum deformation when the external normal and shear force is applied. (e) represents the normal and shear direction stiffness according to the thickness of the flexure structure. (f) is the modal analysis results of the flexure structure.

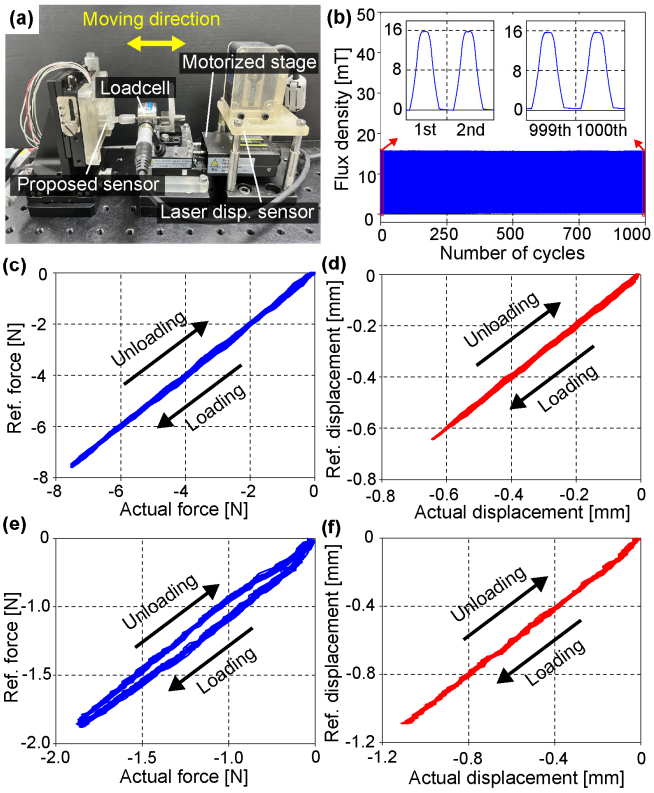

Fig. 4. Experimental evaluation results of the single-cell of the MagTac. (a) is the experimental setup. (b) shows the repeatability test of the sensor in a normal direction over 1,000 cycles. (c) and (d) are the experimental results of the normal direction force and displacement, respectively. (e) and (f) are the results of the shear direction force and displacement, respectively.

characteristic evaluation of the single-cell MagTac sensor is investigated first (see Fig. 2(h-2)). Subsequently the six-axis F/T measurement capability of the MagTac is verified.

A. Experimental Characterization of Single-cell Sensor

To assess the performance of the prototyped single-cell of MagTac sensor, we conducted an experimental evaluation. For the experiment, we construct an experimental bench consisting of a motorized stage (TSDM40-15, SIGMAKOKI), a load cell (LUX-B-50N-ID, KYOWA), and a laser displacement sensor (ZX2-LDA, OMRON) as depicted in Fig. 4(a). In this bench, the load cell is mounted on the motorized stage to measure the amount of applied normal force, and the laser displacement sensor to measure the amount of deformation in the moving direction.

The MagTac sensor configured with the flexure structure has the advantage of a repeatable response to the applied force. To evaluate the repeatability of the MagTac sensor, we conducted the experiment under the experimental bench and the results are shown in Fig. 4(b). After loading a force of 7.2 N and unloading to zero for more than 1,000 cycles, the difference between the maximum and minimum values of magnetic flux density is approximately 2.5 %. From this result, we suggest the proposed sensor is repeatable over 1,000 cycles.

The experimental results in Fig. 4(c) and (d) show that the normal directional force and displacement of the single-cell sensor are highly linear with low errors compared to the reference sensor. The maximum measurement capacity of normal direction force and displacement are 7.6 N and 0.64 mm, respectively. Further, the root mean square error (RMSE) of the force and displacement are calculated as 0.006 N and 0.006 mm each. In the case of the shear directional experiment

TABLE II. SENSING PERFORMANCES OF THE SINGLE-CELL SENSOR

Specifications	Axis		Unit
	Z	*X, Y*	
Force measurement capacity	7.6	1.86	N
RMSE of force	0.006	0.068	
Displacement measurement capacity	0.644	1.112	mm
RMSE of displacement	0.006	0.011	
Max. hysteresis of force	1.875	9.14	% FSO
Max. hysteresis of displacement	2.17	1.28	
Linearity of force and displacement	0.99	0.99	%

as shown in Fig. 4(e) and (f), the displacement of the sensor also shows high linearity. However, the force response of the sensor has the hysteresis loop during the loading and unloading process, where the maximum hysteresis of force is observed as about 9.1 % in the shear direction. The possible cause of this issue is because of the polymeric material of the flexure structure. The measured maximum capacity of the shear direction force and displacement are 1.86 N and 1.11 mm respectively. The calculated RMSE is 0.068 N and 0.011 mm. We further verify the maximum hysteresis and linearity characteristics of the single-cell sensor in normal and shear directions, as tabulated in Table II.

B. Six-axis F/T Measurement Capability

The three normal direction forces and three shear direction forces are necessary to measure the six-axis F/T components. In our MagTac sensor, which is composed of three sensing cells, can measure the three normal forces and six shear forces in total. This implies that the proposed sensor can theoretically measure the six-axis F/T values. In this section, we perform

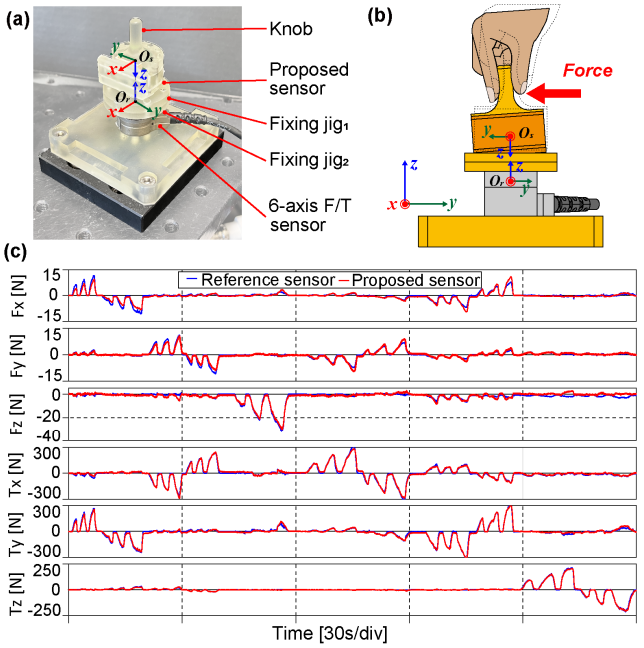

Fig. 5. Experimental performance evaluation of the six-axis F/T measurement capability of the MagTac sensor. (a) and (b) show the calibration and experimental bench and the schematically expressed calibration procedure, respectively. (c) represents the experimental results of the six-axis F/T measurement capability of the proposed MagTac sensor.

TABLE III. SPECIFICATIONS OF THE MAGTAC SENSOR

Specifications	Value		Unit
Number of the sensing cell	3		EA
Weight in total	5.5		g
Overall dimension	23.5×23.5×15		mm
Max. sampling frequency	2000		Hz
Force measurement capacity	- 32 (F_z)	± 15 (F_x,F_y)	N
Average errors of forces	3.15 (F_z)	3.31 (F_x,F_y)	% FSO
Torque measurement range	± 250 (T_z)	± 300 (T_x,T_y)	N·mm
Average errors of torques	0.98 (T_z)	2.88 (T_x,T_y)	% FSO

the calibration and demonstrate its experimental performance to verify the six-axis F/T measurement capability of the proposed sensor.

To evaluate the performance of the six-axis F/T measurement capability of the fully fabricated MagTac sensor, the calibration process is necessary that converts the three-dimensional magnetic flux density measured on each cell of the sensor into the force and torque that is applied to the sensor. For the calibration part, the experimental setup consists of a reference six-axis F/T sensor (Nano17, ATI), two jigs for fixing the reference sensor with the proposed sensor, and a knob as represented in Fig. 5(a). As schematically depicted in Fig. 5(b), the calibration procedure was conducted manually by exerting the external force through the knob fixed on the proposed sensor. The measured magnetic flux density data from each sensing cell, are transferred to a data acquisition microcontroller (STM32F103RET6, STM) via a serial peripheral interface (SPI), and also the measured F/T values of the reference sensor via an external analog to digital converting board (DC682A, Analog Devices) simultaneously.

In this study, we assume that the relationship between the magnetic flux density and the six-axis F/T is linear. This assumption might cause large errors between the reference sensor and the proposed sensor in the calibration process.

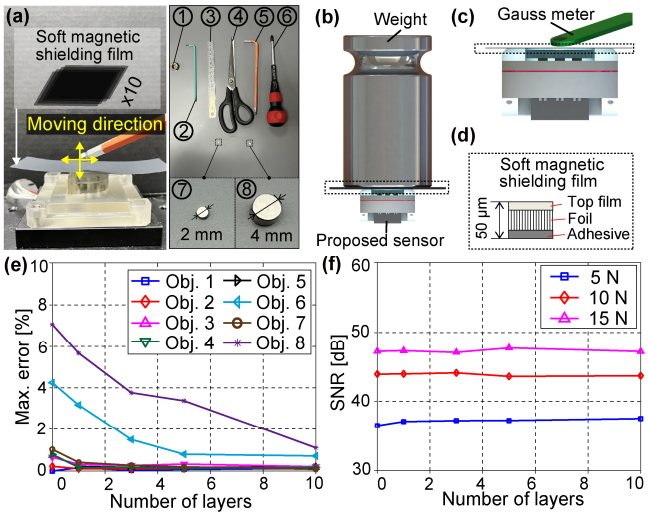

Fig. 6. Feasibility test results of the stray field immunity using the commercial soft magnetic shielding film. (a), (b), and (c) are the experimental setup to verify the effectiveness of the magnetic shielding film. (d) shows the experimental results of the sensing performance of the MagTac sensor related to the number of film layers. (e) indicates the experimental results of the external magnetic field rejection effect according to the number of film layers. (f) represents the sensitivity changes of the proposed sensor according to the number of film layers.

However, we adopt this assumption to simply verify the six-axis F/T measurement capability of the proposed sensor. From the assumption, the relationship between magnetic flux density and F/T is expressed as follows:

$$C \cdot [B_1 B_2 B_3]^T = [F_x F_y F_z T_x T_y T_z]^T \quad (6)$$

where, B_i is the three-dimensional vector of the magnetic flux density that can be expressed as $B_i = [B_{ix}\ B_{iz}\ B_{iz}]^T$. C denotes a 6 × 9 calibration matrix, and $[F_x\ F_y\ F_z\ T_x\ T_y\ T_z]^T$ is the F/T vector measured from the reference sensor. The calibration matrix was obtained using a linear least-squares method as:

$$C = [F_x F_y F_z T_x T_y T_z]^T \cdot [B_1 B_2 B_3]^+ \quad (7)$$

where, $[B_1\ B_2\ B_3]^+$ denotes the pseudo inverse of the three-dimensional vector of the magnetic flux density that can be expressed as $[B_1\ B_2\ B_3]^T([B_1\ B_2\ B_3]\ [B_1\ B_2\ B_3]^T)^{-1}$. Using the (7), the calibration matrix C is obtained.

From obtained calibration matrix, the measured magnetic flux density of the MagTac sensor can be converted to six-axis F/T values. According to the calibration results of the MagTac sensor as presented in Fig. 5(c), results demonstrate that the calibrated value of our proposed sensor generally matched the trend of the reference value. The measured maximum force capacity in the *x*-, *y*-, and *z*-directions are 15, 15, and 32 N, respectively, and the measured maximum torque capacity in *x*-, *y*-, and *z*-directions are 250, 250, and 300 N•mm, respectively. Further, we calculate the average errors of forces and torques. The calculated values and the overall specifications of the MagTac sensor are summarized in Table III.

IV. STRAY MAGNETIC FIELD IMMUNITY OF MAGTAC SENSOR

The hall-effect-based tactile sensor is commonly known to have great influence by the external stray field. This is a critical problem when the robot performs various tasks in an

unstructured environment. One of the methods to have immunity to the external stray magnetic field, is adopting a gradiometric-based external stray field cancellation method as proposed in [17]. However, there still lies problems in interacting with the ferromagnetic material due to the neodymium magnet on the top of the soft sensor which reacts to the ferromagnetic materials. To overcome these problems, we utilize the off-the-shelf shielding film (EM80KM-005-1, 3M) and verify its effectiveness as shown in Fig. 6.

To quantitatively demonstrate the shielding effect of the film, we prepare 10 films and test objects as in Fig. 6 (a). In preparing the objects, we first measure the magnetic flux density of the objects using the Gauss meter (TM-801, KANETAC), and the measured magnetic flux densities of objects are 5, 19, 24, 48, 56, 165, 1681, and 3370 G, respectively. Fig. 6(e) shows the maximum error of the sensor data caused by the magnetized objects in accordance with the number of films. The experimental results demonstrate that the proposed method can effectively shield even with the relatively large external stray magnetic field. We used ten film layers in this study to have minimum error and the total thickness is only about 500 μm as shown in Fig. 6(d).

Although the MagTac sensor has a relatively large distance between the sensing plate and the neodymium magnet, the magnetic field could be detected on the top of the sensing plate, and this can consequently affect the object. In order to test whether the magnetic film can shield this magnetic effect, we manually measure the magnetic flux density according to the number of layers of magnetic film as shown in Fig. 6(c). In the case without the film, the magnetic flux density was measured at about 10 G. However it decreases to zero even with the single film.

To verify whether the film affects the sensitivity of the MagTac sensor, we measure the signal-to-noise ratio (SNR) with three different masses according to the number of film layers as shown in Fig. 6(b) and (f). The experimental results show that the soft magnetic shielding film merely not affects the performance of the sensor.

V. Conclusion

In this work, we develop the hall-effect-based fingertip tactile sensor capable of measuring the six-axis F/T and immune to the external stray magnetic field. Based on the three-axis force sensing mechanism using pillar and flexure structures, the MagTac sensor is designed to measure the six-axis F/T value. In addition, the sensing performance and immunity to the external magnetic field of the proposed sensor were demonstrated by experiments.

In future works, we will focus on improving the sensing performance of the MagTac sensor. Firstly, we will optimally design the flexure structure in order to enhance the sensitivity; and reduce the hysteresis in the shear direction considering the material and fabrication of the flexure structure. Secondly, based on the high bandwidth characteristic of the MagTac sensor, the linear and rotational slip detection ability by analyzing the frequency response will be developed. Moreover, we will verify the decoupling capability of the sensor by utilizing the motorized experimental test bench.

References

[1] A. Saxena *et al.*, “Robotic grasping of novel objects using vision,” *Int. J. Robot. Res.*, vol. 27, no. 2, pp. 157-173, Feb.2008.

[2] F. Ficuciello *et al.*, “Vision-based grasp learning of an anthropomorphic hand-arm system in a synergy-based control framework,” *Sci. Robot.*, vol. 4, no. 26, Jan. 2019.

[3] Y. She *et al.*, “Cable manipulation with a tactile-reactive gripper,” *Int. J. Robot. Res.*, vol. 40, no. 12-14, pp. 1385-1401, 2021.

[4] F.R. Hogan *et al.*, "DIGIT: A Novel Design for a Low-Cost Compact High-Resolution Tactile Sensor With Application to In-Hand Manipulation," *IEEE Robot.Autom. Lett.*, vol. 5, no. 3, pp. 3838-3845, July 2020.

[5] S. Park and D. Hwang, "Softness-Adaptive Pinch-Grasp Strategy Using Fingertip Tactile Information of Robot Hand," *IEEE Robot.Autom. Lett.*, vol. 6, no. 4, pp. 6370-6377, Oct. 2021.

[6] T. M. Huh *et al.*, "Dynamically Reconfigurable Tactile Sensor for Robotic Manipulation," *IEEE Robot.Autom. Lett.,* vol. 5, no. 2, pp. 2562-2569, April 2020.

[7] M. Ohka *et al.*, "Optical Three-Axis Tactile Sensor for Robotic Fingers", in Sensors: Focus on Tactile Force and Stress Sensors. London, United Kingdom: IntechOpen, 2008.

[8] H. Sun *et al.*, "A soft thumb-sized vision-based sensor with accurate all-round force perception," *Nature Machine Intelligence.,* vol. 4, no. 2, pp. 135-145, 2022.

[9] H. Khamis *et al.*, " A novel optical 3D force and displacement sensor–Towards instrumenting the PapillArray tactile sensor,” *Sensors and Actuators A: Physical*, vol. 291, no. 2, pp. 174-187, 2019.

[10] T. Taunyazov *et al.*, "Event-driven visual-tactile sensing and learning for robots," *arXiv preprint arXiv:2009.07083*, 2020.

[11] Z. Lu *et al.*, "GTac: A Biomimetic Tactile Sensor With Skin-Like Heterogeneous Force Feedback for Robots," *IEEE Sens. J.*, vol. 22, no. 14, pp. 14491-14500, July 2022.

[12] Y. Yan *et al.*, “Soft magnetic skin for super-resolution tactile sensing with force self-decoupling,” *Sci. Robot.*, vol. 6, no. 51, Jan. 2021.

[13] T. Hellebrekers *et al.*, "Soft Magnetic Tactile Skin for Continuous Force and Location Estimation Using Neural Networks," *IEEE Robot.Autom. Lett.*, vol. 5, no. 3, pp. 3892-3898, July 2020.

[14] T. Kawasetsu *et al.*, “Mexican-hat-like response in a flexible tactile sensor using a magnetorheological elastomer,” *Sensors*, vol. 18, no. 2, 2018.

[15] A. Mohammadi *et al.*, "Flexible mechanical metamaterials enabling soft tactile sensors with multiple sensitivities at multiple force sensing ranges," *Scientific reports*, vol. 11, no. 1, pp. 1-9, July 2021.

[16] E. Harber *et al.*, "A Tunable Magnet-based Tactile Sensor Framework," *2020 IEEE SENSORS*, pp. 1-4, 2020.

[17] T. Le Signor *et al.*, "A Gradiometric Magnetic Force Sensor Immune to Stray Magnetic Fields for Robotic Hands and Grippers," *IEEE Robot.Autom. Lett.*, vol. 7, no. 2, pp. 3070-3076, April 2022.

[18] M. Rehan *et al.*, “A Soft Multi-Axis High Force Range Magnetic Tactile Sensor for Force Feedback in Robotic Surgical Systems,” *Sensors*, vol. 22, no. 9, 2022.

[19] H. Wang *et al.*, “Design methodology for magnetic field-based soft tri-axis tactile sensors,” *Sensors*, vol. 16, no. 9, 2016.

[20] K. Dai et al., "Design of a Biomimetic Tactile Sensor for Material Classification," 2022 International Conference on Robotics and Automation (ICRA), pp. 10774-10780, 2022.

[21] A. Mohammadi *et al.*, “Magnetic-based soft tactile sensors with deformable continuous force transfer medium for resolving contact locations in robotic grasping and manipulation,” *Sensors*, vol. 19, no. 22, 2019.

[22] T. P. Tomo *et al.*, "A New Silicone Structure for uSkin—A Soft, Distributed, Digital 3-Axis Skin Sensor and Its Integration on the Humanoid Robot iCub," *IEEE Robot.Autom. Lett*, vol. 3, no. 3, pp. 2584-2591, July 2018.

[23] S. Awtar and A. Slocum*“*Flexure systems based on a symmetric diaphragm flexure,” in *Proc. of the ASPE 2005 Annual Meeting.* Norfolk, VA, Paper No. 18003, 2005.

[24] W. C. Young, R. G. Budynas, and A. M. Sadegh, *Roark’s formulas for stress and strain*, McGaw-Hill Education, New York, 2012.